Taylor & Francis
Taylor & Francis Group

Philosophical Magazine Letters

ISSN: 0950-0839 (Print) 1362-3036 (Online) Journal homepage: http://www.tandfonline.com/loi/tphl20

NiTi superelasticity via atomistic simulations

Piyas Chowdhury, Guowu Ren & Huseyin Sehitoglu

To cite this article: Piyas Chowdhury, Guowu Ren & Huseyin Sehitoglu (2015) NiTi superelasticity via atomistic simulations, Philosophical Magazine Letters, 95:12, 574-586, DOI: 10.1080/09500839.2015.1123819

To link to this article: http://dx.doi.org/10.1080/09500839.2015.1123819

Published online: 22 Dec 2015.

Philosophical Magazine Letters, 2015
Vol. 95, No. 12, 574–586, http://dx.doi.org/10.1080/09500839.2015.1123819

NiTi superelasticity via atomistic simulations

Piyas Chowdhury[a], Guowu Ren[b] and Huseyin Sehitoglu[a]*

[a]*Department of Mechanical Science and Engineering, University of Illinois at Urbana-Champaign, 1206 W. Green St., Urbana, IL 61801, USA;* [b]*Institute of Fluid Physics, China Academy of Engineering Physics, Mianyang 621999, China*

(*Received 21 May 2015; accepted 19 November 2015*)

The NiTi shape memory alloys (SMAs) are promising candidates for the next-generation multifunctional materials. These materials are superelastic i.e. they can fully recover their original shape even after fairly large inelastic deformations once the mechanical forces are removed. The superelasticity reportedly stems from atomic scale crystal transformations. However, very few computer simulations have emerged, elucidating the transformation mechanisms at the discrete lattice level, which underlie the extraordinary strain recoverability. Here, we conduct breakthrough molecular dynamics modelling on the superelastic behaviour of the NiTi single crystals, and unravel the atomistic genesis thereof. The deformation recovery is clearly traced to the reversible transformation between austenite and martensite crystals through simulations. We examine the mechanistic origin of the tension–compression asymmetries and the effects of pressure/temperature/strain rate variation isolatedly. Hence, this work essentially brings a new dimension to probing the NiTi performance based on the mesoscale physics under more complicated thermo-mechanical loading scenarios.

Keywords: superelasticity; phase transformation; atomic structure; molecular dynamics; computer simulations

Background

Since the discovery in 1960s [1], NiTi SMAs have found widespread commercial usage in biomedical, aerospace and automotive industries today [2,3]. There have been a considerable number of experimental [4,5] and theoretical undertakings ever since to rationalize the unique pseudoelastic attributes therein on physical basis (Figure 1). On theoretical grounds, the last decade has witnessed significant progresses in terms of advancing from phenomenological continuum modelling [6–8] into the atomic scale approaches [9,10]. Atomistically, two distinct classes of theories can be noted, namely, the quantum mechanical predictions of lattice properties (e.g. the elastic moduli, the transformation energy pathways) and mesoscale deformation simulations. While very informative, the *ab initio* methods are confined to only tens of atoms (due to a rather rigorous requirement of computational capability [11,12]). By contrast, molecular dynamics (MD) simulations can address mesoscale crystals (consisting of millions of atoms) by utilizing pair potential-based descriptions. This letter documents such

*Corresponding author. Email: huseyin@illinois.edu

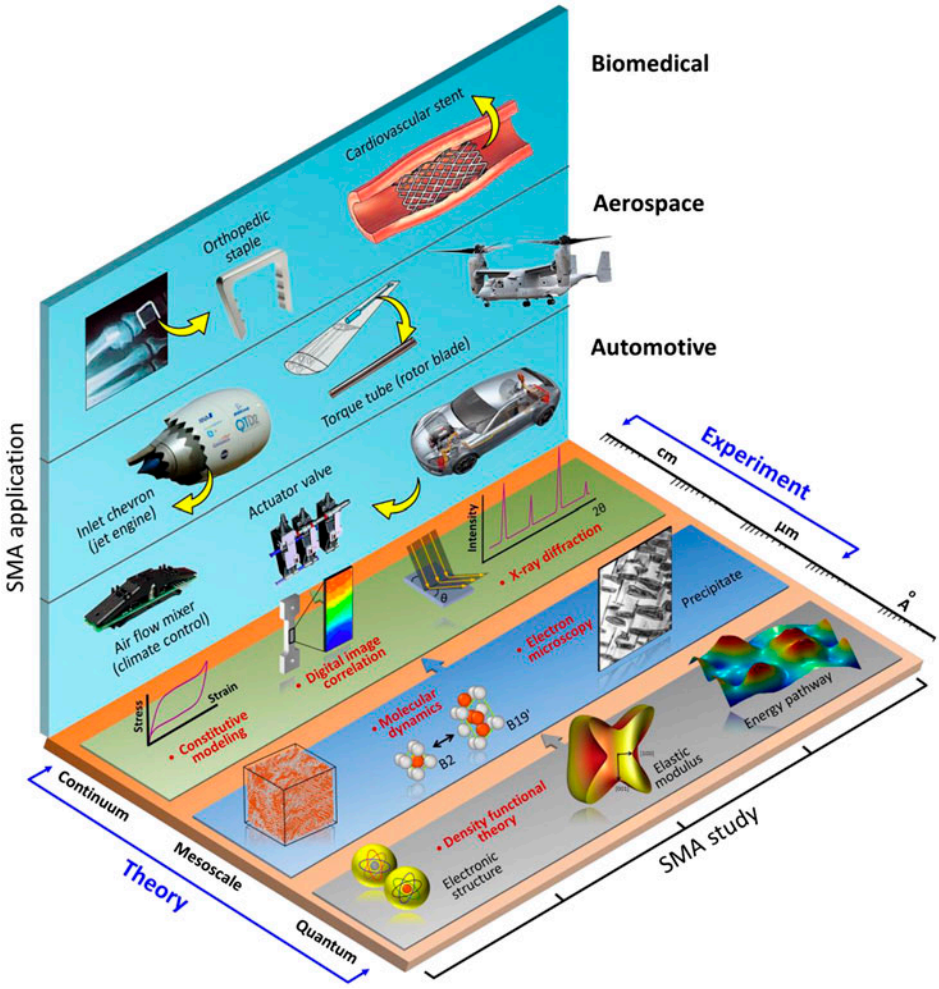

Figure 1. A schematic illustration of some select applications of the NiTi based SMAs, and the study of the associated physics spanning various length scales.

predictions of phase transformations and accurate constitutive response with the aid of a newly developed potential.

MD studies using previously developed potentials on NiTi SMAs [13–16] have been able to predict various interesting aspects of NiTi behaviours at the lattice scale. For instance, Farkas et al. [13] predicted the B2 lattice cohesive energy. Subsequently, Lai and Liu theorized the melting behaviour thereof using a new potential. Most recently, Zhu and co-workers [15,17] further modified Lai's potential to study martensitic phase transformation. Independently, Mutter and Nielaba [16,18] improved Lai's original potential to model temperature/composition-dependent transformation. In view of the literature findings, we note that the central features of NiTi SMAs to be modelled are essentially threefold: (a) the correct shape and magnitudes of stress–strain hysteresis loops (i.e. comparable to experimental ones), (b) the reversibility of martensitic phase

transformation (i.e. B2 ↔ B19′) and (c) the stability of individual phases subjected to stress and temperature variations. As experimental literature noted, NiTi SMAs possess distinctive mechanical traits such as strong tension–compression asymmetry, dependence of hydrostatic stress and temperature, the origin of which merits rigorous atomistic rationalizations. While the previous models were successful in capturing various crystal level responses, there still exists a need for predicting the full spectrum of the NiTi constitutive attributes using a single potential. Utilizing the literature knowledge, we adopt several improvement strategies in the form of fine-tuning the cut-off sensitivity and accurately fitting the cross-interaction energy terms to better describe the material potential energy landscape (see Appendix 1). As a result, we set out to address the inherently complex NiTi constitutive behaviours under various thermo-mechanical conditions, using extensive MD simulations.

Model description

The austenitic NiTi single crystals of CsCl-type unit cells were constructed using the basis: Ni ≡ (0 0 0) and Ti ≡ (0.5 0.5 0.5). The size of the cubic crystal (with each side being 30 nm) is selected based on the convergence of physical observables (e.g. temperature, pressure, kinetic and potential energy) to the system size independence. The crystals represent bulk material (i.e. without any free surface or dangling bonds) as ascertained by enforcing periodic boundary condition on the crystal facets [19]. The number of atoms in a typical simulation supercell was about 3×10^5, which is sufficiently large to avoid any size- and/or periodicity-induced artefacts. The stress–strain responses reported in this letter are computed based on the concept of virial stress (which is the atomistically equivalent quantity of the conventional Cauchy stress).

Energetically minimized defect-free bulk B2 crystal structure is characterized by its distinctive CsCl-type unit cell with a lattice constant, $a_{B2} = 3.021$ Å in Figure 2a. We have selected the $\langle 0\,1\,1 \rangle_{B2}$ crystallographic orientation along which to apply loads. Choosing one particular orientation is important for consistency due to the strong orientation dependence of the NiTi superelastic response [20].

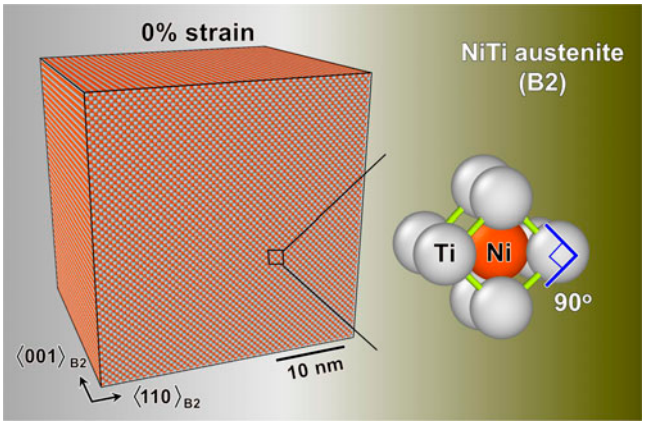

Figure 2a. Single crystal NiTi at the austenite phase (B2) prior to any deformatoin (i.e. at 0% strain). The unit cell structure is of CsCl type.

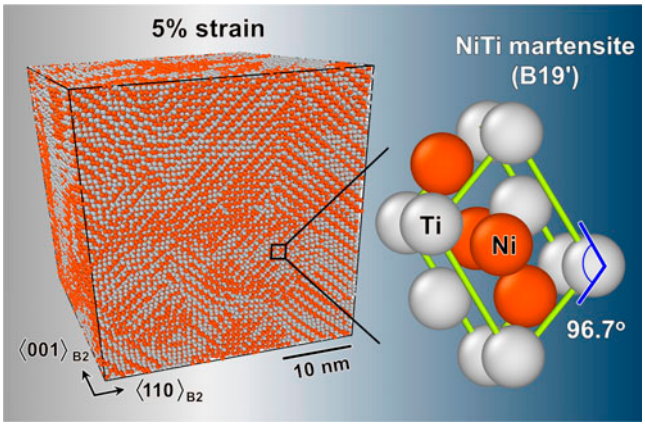

Figure 2b. The NiTi martensite (B19′ crystal) at 5% strain (notice the internally twinned strcture). The B19′ unit cell structure is monoclinic with one angle of the unit cell being non-right angled.

On deforming to 5% strain, the B2 phase fully transforms into a martensitic material (i.e. B19′ phase) as shown in Figure 2b. The primitive unit cell of the B19′ crystal is of monoclinic type with the lattice variables: $a_{B19'} = 4.606$ Å, $b_{B19'} = 4.386$ Å, $c_{B19'} = 2.699$ Å and $\alpha_{B19'} = \gamma_{B19'} = 90° < \beta_{B19'}$ (≈96.7°). During the deformation simulations, the austenite and the martensite phases are identified by their distinctive unit cells.

Results and discussion

First, we examine the superelastic load–unload behaviours under compression and tension. Figures 3a and 3b present the respective stress–strain curves (at 300 K temperature), and illustrate the governing atomistic mechanism step by step. In the following discussion, we describe the compression case in full details. Then we analyse the mechanistic foundation of the observed tension and compression asymmetries. In Figure 3a, the austenitic NiTi deforms elastically along the linearly rising stress–strain curve (from 0% strain up to 1.8%). During this period, the crystal phase remains the same as the initial B2 structure. On reaching a critical stress level of 776 MPa (i.e. the 'transformation stress', the experimental value of which is about 800 MPa [20]), the B2 austenite starts to transform into B19′ martensite in various regions of the parent crystal. At this stage, three simultaneous atomistic processes are observed to be happening. Firstly, the atoms, that constitute the original CsCl-type B2 lattice, start rearranging into the monoclinic B19′ lattice. Secondly, the atoms, part of the newly transformed martensite lattice, undergo ordering among themselves to create multiple mirrored strips (a phenomenon known as the 'internal twinning' of the martensite). Such twinning process is designated as the 'compound type' prevailing on the {0 0 1} family of planes. And thirdly, further loading continues to produce the deformation twins on the {0 0 1} systems, extending to high strains. The single crystal becomes fully martensitic at 4% strain. This behaviour is consistent with early experiments [20]. Continuation of applied force results in the elastic distortion of the twinned martensite, corresponding to the rise of stress–strain curve (from 4% up to 5% strain). No significant structural modification is discerned due to the

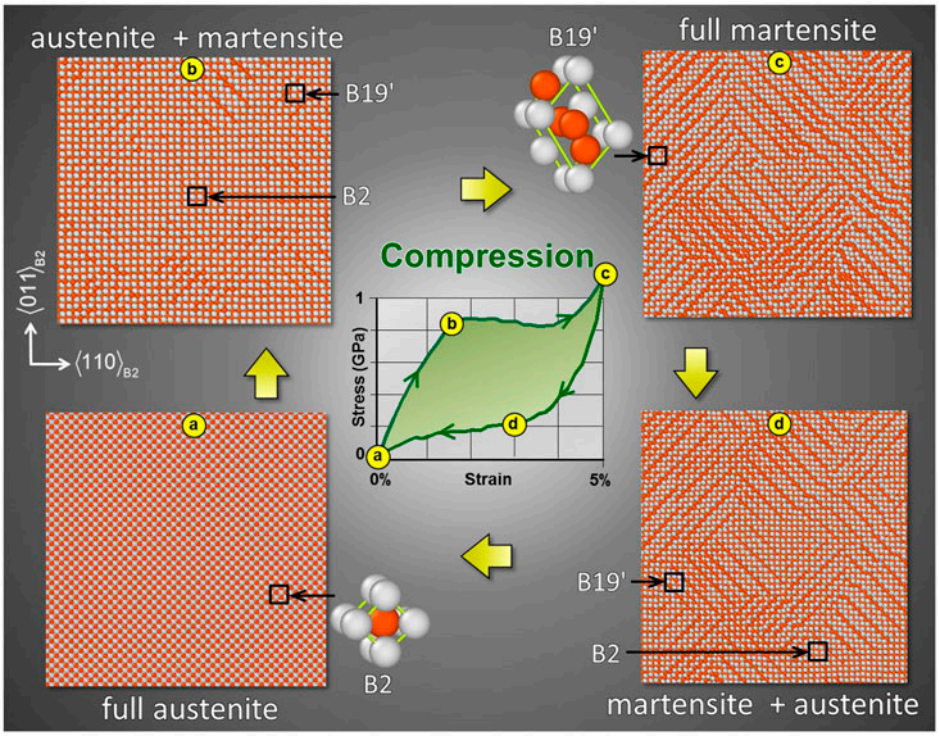

Figure 3a. Superelasticity of NiTi under $\langle 0\,1\,1\rangle_{B2}$ compression and at 300 K. Notice the reversible austenite (B2) ↔ martensite (B19′) transformation.

elastic straining of martensite. The final atomic structure at the end of loading (at 5% strain) is characterized by multiple internal twins (made of monoclinic unit cells).

On full unloading, the deformed crystal completely reverts back to its initial undeformed state (i.e. the B2 austenite at 0% strain) as in Figure 3a. Mechanistically, the martensite first undergoes elastic recovery (from 5 to 4.2% strain). Then, the reverse transformation process is initiated i.e. the martensite starts returning to austenite, marked by the beginning of the lower stress plateau. The phenomenon implies that the internally twinned B19′ structure is stable only under high stress, and hence the removal of stress triggers the reverse B19′-to-B2 transformation. The volume fraction of the martensitic B19′ phase continuously decreases along the stress plateau. After complete unloading, the material retains no residual martensite and hence no residual strain/stress. The transformation strain i.e. the total strain (5%) minus the elastic strain (about 0.8%) is calculated to be about 4.2% (which is experimentally reported to be around 5% [21]). As noted in the early literature, higher transformation strain can result if one variant growth is occurring in the expense of others i.e. detwinning [22]. By contrast, crystals with multiple twins promote reduced transformation strain. In the current case, the presence of multiple variants (i.e. internally twinned structure) is strongly believed to be the reason for the slightly lower predictions than the experiments.

The tensile behaviour is superelastic, however, with reduced hysteresis area as shown in Figure 3b. The corresponding transformation stress is determined to be about 720 MPa

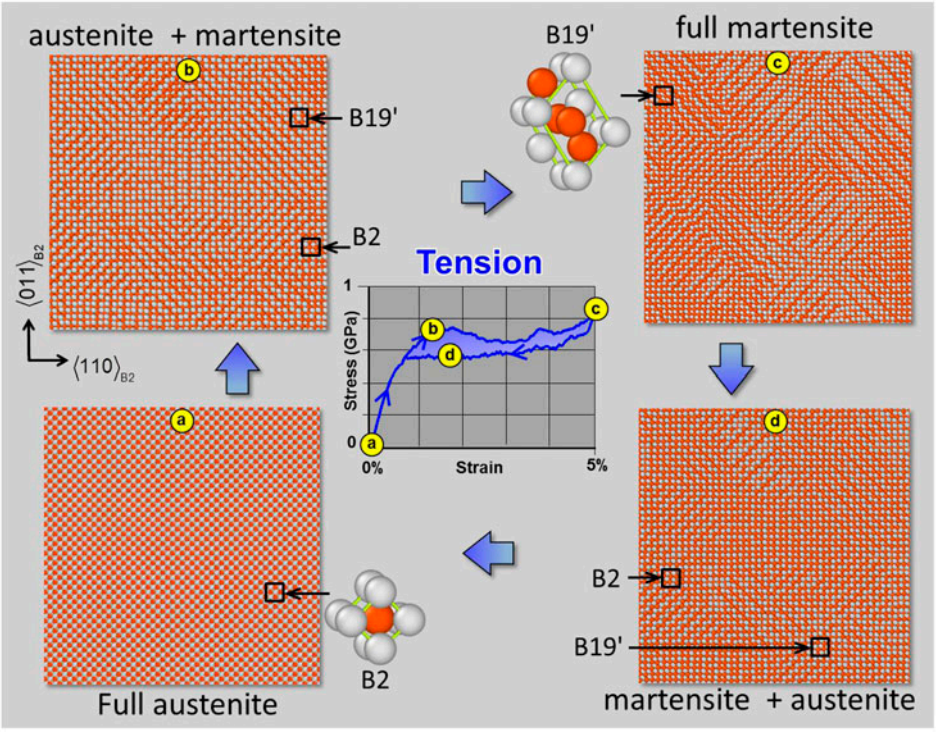

Figure 3b. Tensile strain behaviour at 300 K for $\langle 0\,1\,1 \rangle_{B2}$ loading orientation.

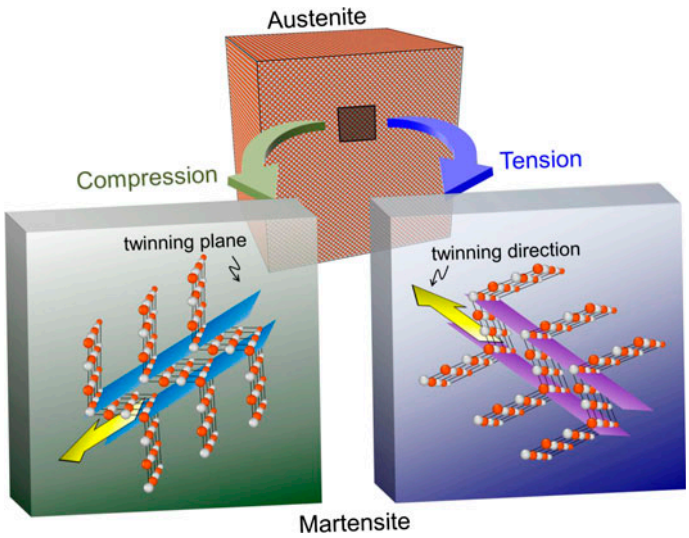

Figure 3c. Different twinning systems activated under compression/tension due to the unidirectional nature of deformation twinning, thereby giving rise to the constitutive asymmetries.

(matching with early experiments [20,21]). The asymmetric deformation behaviour in tension/compression can be clarified upon carefully examining the deformed atomistic structures under the two loading modes. The observed stress–strain asymmetries can be interpreted as the natural outcome of the very 'uni-directional' nature of the deformation twinning. The process of twinning occurs on a very specific set of crystallographic planes as well as along a unidirectionally preferred sense [23] (also known as the 'transformation direction'). That is to say, if the resolved shear stress along a certain transformation direction triggers twinning, the 180°-opposite transformation direction is unfavourable for such process as schematically illustrated in Figure 3c. Therefore, under the compression and tension, phase transformation occurs on different sets of planes and directions in Figures 3a and 3b insets. As a result, the apparent asymmetries in the transformation stresses and in the overall constitutive hysteresis arise for different loading senses.

Most interestingly, regardless of high strain rates (inherent in all MD simulations), the predicted transformation stresses are found remarkably close to the typical experimental values [20,21]. This finding has very important mechanistic implications. Experimentally, high strain rates cause increased hysteresis and eventually loss of superelasticity due to: (a) nucleation of dislocation slip in the austenitic phase [24] and (b) preclusion of deformation-generated heat flow [25]. However, the current MD deformation proceeds only via twinning of the B19′ lattice with no slip activities whatsoever. Reportedly, pure twinning has very low-rate dependence as opposed to the slip activities [26]. Moreover, the heat flow rate is in synchronization with the deformation rates in the simulations, thereby producing no adiabatic side effect. In other words, the simulated deformation scenario is mechanistically equivalent to the experimental low-rate constitutive response governed solely by deformation twinning. Therefore, the present transformation stress levels as well as the hysteresis loops are rate insensitive (as cross-validated by conducting multiple

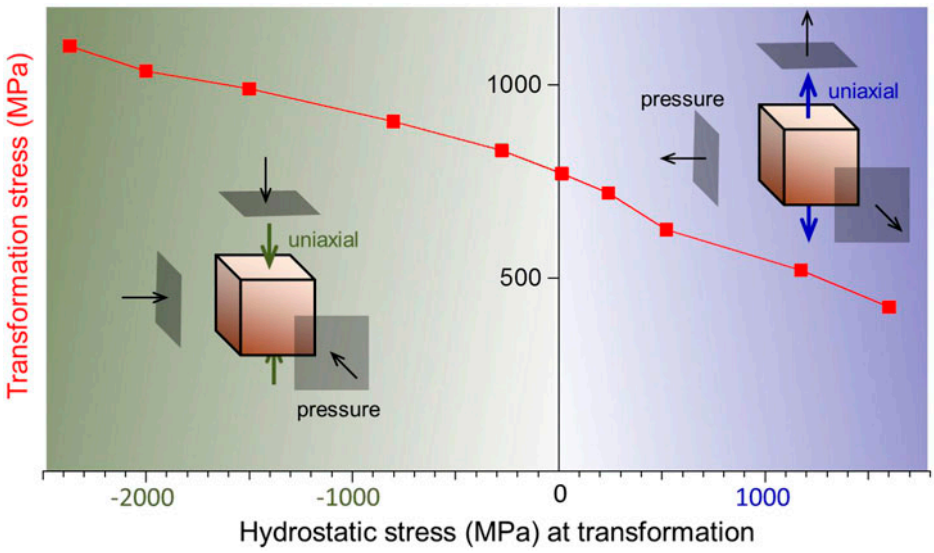

Figure 4a. Variation in $\sigma_{\text{transform}}$ under hydrostatic stress, $\sigma_{\text{hydrostatic}} = \frac{\pm\sigma_{\text{transform}}}{3} - P_{\text{external}}$ (externally applied pressure, P_{external} is positive if compressive while $\sigma_{\text{transform}}$ is positive if tensile). Note only absolute magnitude of $\sigma_{\text{transform}}$ is however plotted for the convenience of showing the trend.

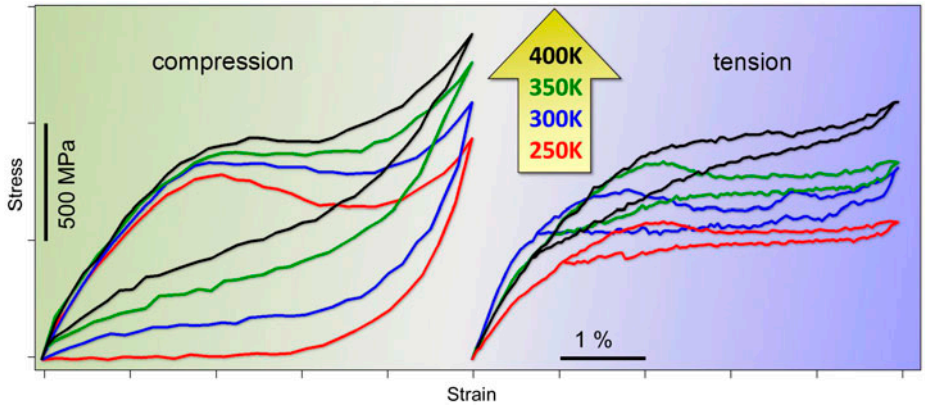

Figure 4b. Temperature dependence of the stress–strain curves for NiTi under compression and tension along $\langle 0\,1\,1\}\rangle_{B2}$ orientation. At higher temperature (> 450 K), the NiTi alloy loses superelastic behaviour.

simulations). Nonetheless, the transformation behaviour is observed to be strongly affected by the variation in ambient pressure and temperature.

External pressure quite strongly modifies the NiTi phase transformation behaviour, the origin of which is traced to the crystallography of deformation. The martensitic transformation under the tensile (i.e. positive) hydrostatic stress is demonstrably favoured over the compression case as in Figure 4a. This behaviour has been documented experimentally [27]; however, the physical clarification thereof has remained elusive so far. As per the present simulations, the pressure effects can be attributed to the twinning unidirectionality as explained earlier in Figure 3c. Inherently, a parent austenitic crystal has 24 sets of planes and directions to create a twin–matrix pair (i.e. the so-called 'variant') during transformation. Various hydrostatic stress states (tension or compression) activate multiple variants in different numbers and senses. Therefore, increasing compressive pressure makes the phase transformation process more and more difficult due solely to the various number of active variants.

On the other hand, the temperature dependency of the NiTi superelasticity is also an interesting phenomenon. Figure 4b demonstrates that higher temperatures (250 K → 300 K → 350 K → 400 K) raise both the lower and upper stress plateaus of the stress–strain hysteresis. This trend agrees with the earlier experimental observations [28] as well as the thermodynamics of transforming alloys [8]. Curiously, this behaviour is quite unlike any conventional alloys, which experience decreasing plastic stress levels with rising temperatures. The temperature effects on the NiTi alloy can be rationalized by the fact that the monoclinic B19′ structure (constituting the martensite phase) becomes unstable at elevated temperatures. As a result, the austenite-to-martensite transformation becomes more difficult to occur, necessitating additional applied mechanical forces. Simulationwise, a gradually decreasing volume fraction of the martensitic crystal is noticed at the end of loading (at 5% strain) at higher temperatures. Moreover, above 450 K, the original austenitic B2 crystal starts to behave like a common alloy (i.e. undergoes temperature-dependent plastic deformation without any phase transformation), no longer displaying the superelastic properties.

Conclusions and future research

In summary, we have captured: (i) the reversible B2 ↔ B19′ phase changes affecting the NiTi stress–strain behaviour, (ii) the tension/compression asymmetries and the associated transformation stresses and strains, (ii) the correct lattice constants and angles for B2 and B19′ phases, (iii) the internal twinning planes of martensite, (iv) the atomistic foundation of the strain rate, temperature and pressure dependence. However, the true merit of the current modelling endeavour lies at the vast promise that it holds in the realm of computational materials science. With the exponentially increasing microprocessor power (following the Moore's law), today we are in a position to advance the existing computational tools to explore the theoretical territories beyond the experimental capacity. To that end, we offer a milestone in predicting the atomistic origin of the superelasticity using NiTi as the representative SMA. This work essentially lays the groundwork for employing computer simulations to address additional problems such as fracture and fatigue. For instance, discrete lattice simulations can be used to study the crack-tip phenomena under static fracture or fatigue condition as has been shown by the authors previously [29]. The poor fatigue and fracture performances are at present a major setback for further extending the NiTi SMA usage [30] as demonstrated experimentally. Thus, utilizing important atomistic input, accurate prediction of the continuum damage properties could be established [31], a knowledge which would be invaluable for designing better SMAs in the future. Furthermore, understanding the role of coherent Ni_4Ti_3 precipitates [32,33] is an ongoing research pursuit, which also can benefit immensely from mesoscale simulations.

Acknowledgements

We acknowledge the use of the parallel computing resource, the Taub cluster, at the University of Illinois. The picture courtesies of the NiTi SMA applications are:

(1) Cardiovascular stent – http://www.britannica.com/EBchecked/topic/24,387/aneurysm/images-videos/106,616/coronary-artery-insertion-of-a-stent-into-a-coronary-artery%29.
(2) X-ray image of orthopaedic staple – http://www.nitifrance.com/osteosynthesis-staples.php.
(3) Orthopaedic staple – http://www.vilex.com/vilex-surgical-products/vilex-memory-staple-system/pdf/Staple%20Sheet_1-23-14.pdf.
(4) Inlet chevron for jet engine - http://www.grc.nasa.gov/WWW/StructuresMaterials/AdvMet/research/shape_memory.html.
(5) Tilt-rotor V 22 Osprey aircraft – http://www.boeing.com/defense/v-22-osprey/.
(6) The V 22 Osprey torque tube pictures are taken from the paper by Mabe et al. [34].
(7) See-through car – http://www.italiantestdriver.com/wp-content/gallery/porsche-panamera-sport-turismo-concept/porsche-panamera-sport-turismo-concept-8.jpg.
(8) Actuator valve – http://www.actuatorsolutions.de/products/valves/air-gas/33-module-as8p/.
(9) Air flow mixer (climate control) – http://www.pointex.eu/upload/2013_07_16_Innovation_Day/presentazione_BUTERA-SAES.pdf.

Funding

This research was supported by the Nyquist chair funds.

Supplemental data

The supplemental video for this article can be accessed at http://dx.doi.org/10.1080/09500839.2015.1123819

References

[1] F.E. Wang, W.J. Buehler and S.J. Pickart, J. Appl. Phys. 36 (1965) p.3232.
[2] L.M. Schetky, Sci. Am. 241 (1979) p.74.
[3] K. Yamauchi, I. Ohkata, K. Tsuchiya and S. Miyazaki, *Shape Memory and Superelastic Alloys*, Elsevier, Cambridge, 2011.
[4] Y. Kudoh, M. Tokonami, S. Miyazaki and K. Otsuka, Acta Metall. 33 (1985) p.2049.
[5] C. Efstathiou, H. Sehitoglu, J. Carroll, J. Lambros and H. Maier, Acta Mater. 56 (2008) p.3791.
[6] E. Patoor, A. Eberhardt and M. Berveiller, Le J. Phys. IV 6 (1996) p.C1.
[7] K. Bhattacharya, *Microstructure of Martensite: Why it Forms and How it Gives Rise to the Shape-Memory Effect*, Vol. 2, Oxford University Press, Oxford, 2003.
[8] J.G. Boyd and D.C. Lagoudas, Int. J. Plast. 12 (1996) p.805.
[9] X. Huang, G.J. Ackland and K.M. Rabe, Nat. Mater. 2 (2003) p.307.
[10] M.-X. Wagner and W. Windl, Acta Mater. 56 (2008) p.6232.
[11] P. Chowdhury, H. Sehitoglu, W. Abuzaid and H. Maier, Int J. Plast. 71 (2015) p.32.
[12] P.Chowdhury, H.Sehitoglu, H.Maier and R.Rateick, Int. J. Plast. (2015). doi: 10.1016/j.ijplas.2015.07.002
[13] D. Farkas, D. Roqueta, A. Vilette and K. Ternes, Modell. Simul. Mater. Sci. Eng. 4 (1996) p.359.
[14] W. Lai and B. Liu, J. Phys.: Condens. Matter 12 (2000) p.L53.
[15] Y. Zhong, K. Gall and T. Zhu, Acta Mater. 60 (2012) p.6301.
[16] D. Mutter and P. Nielaba, Eur. Phys. J. B 84 (2011) p.109.
[17] R. Mirzaeifar, K. Gall, T. Zhu, A. Yavari and R. DesRoches, J. Appl. Phys. 115 (2014) p.194307.
[18] D. Mutter and P. Nielaba, J. Alloys Compd. 577 (2013) p.S83.
[19] P.B. Chowdhury, H. Sehitoglu, R.G. Rateick and H.J. Maier, Acta Mater. 61 (2013) p.2531.
[20] H. Sehitoglu, J. Jun, X. Zhang, I. Karaman, Y. Chumlyakov, H. Maier and K. Gall, Acta Mater. 49 (2001) p.3609.
[21] L. Orgéas and D. Favier, Acta Mater. 46 (1998) p.5579.
[22] H. Sehitoglu, R. Hamilton, D. Canadinc, X. Zhang, K. Gall, I. Karaman, Y. Chumlyakov and H. Maier, Metall. Mater. Trans. A 34 (2003) p.5.
[23] J.W. Christian and S. Mahajan, Prog. Mater. Sci. 39 (1995) p.1.
[24] S. Nemat-Nasser, J.-Y. Choi, W.-G. Guo and J.B. Isaacs, Mech. Mater. 37 (2005) p.287.
[25] P.H. Leo, T. Shield and O.P. Bruno, Acta Metall. Mater. 41 (1993) p.2477.
[26] M. Meyers, O. Vöhringer and V. Lubarda, Acta Mater. 49 (2001) p.4025.
[27] K. Jacobus, H. Sehitoglu and M. Balzer, Metall. Mater. Trans. A 27 (1996) p.3066.
[28] K. Otsuka and X. Ren, Prog. Mater. Sci. 50 (2005) p.511.
[29] P.B. Chowdhury, H. Sehitoglu and R.G. Rateick, Int. J. Fatigue 68 (2014) p.277.
[30] S. Robertson, A. Pelton and R. Ritchie, Int. Mater. Rev. 57 (2012) p.1.
[31] P.B. Chowdhury, H. Sehitoglu and R.G. Rateick, Int. J. Fatigue 68 (2014) p.292.

[32] K. Gall, H. Sehitoglu, Y.I. Chumlyakov and I. Kireeva, Acta Mater. 47 (1999) p.1203.
[33] W. Tirry and D. Schryvers, Acta Mater. 53 (2005) p.1041.
[34] J.H. Mabe, R.T. Ruggeri, E. Rosenzweig and M.Y. Chin-Jye, *NiTinol Performance Characterization and Rotary Actuator Design, in Smart Structures and Materials*, International Society for Optics and Photonics, San Diego, CA, 2004, p.95.
[35] R.R. Zope and Y. Mishin, Phys. Rev. B 68 (2003) p.024102.
[36] Y. Mishin, Acta Mater. 52 (2004) p.1451.
[37] P. Giannozzi, S. Baroni, N. Bonini, M. Calandra, R. Car, C. Cavazzoni, D. Ceresoli, G.L. Chiarotti, M. Cococcioni and I. Dabo, J. Phys.: Condens. Matter 21 (2009) p.395502.
[38] O. Mercier, K. Melton, G. Gremaud and J. Hägi, J. Appl. Phys. 51 (1980) p.1833.
[39] J. Wang and H. Sehitoglu, Int. J. Plast. 61 (2014) p.17.
[40] S. Plimpton, J. Comput. Phys. 117 (1995) p.1.
[41] A. Stukowski, Modell. Simul. Mater. Sci. Eng. 18 (2010) p.015012.
[42] P.B. Chowdhury, *Fatigue Crack Growth (FCG) Modeling in the Presence of Nano-obstacles*, University of Illinois at Urbana-Champaign, Urbana, 2011.

Appendix 1. Constructing pair potential

We provide a brief account of the current MD potential development procedure. The full description covers considerable details and hence constitutes the topic of another paper By G. Ren and H. Sehitoglu (to be published). In Finnis–Sinclair formalism, the total potential energy of a metallic lattice, U_{total}, can be written as:

$$U_{\text{total}} = \sum_{\substack{i,j \\ i\neq j}} \phi_{\text{ij}} + \sum_{\substack{i \\ i\neq j}} F_i \left(\sum_{\substack{j \\ j\neq i}} \rho_{\text{ij}} \right) \tag{1}$$

where i and j represent atoms; $\phi_{\text{ij}} = \phi_{\text{ij}}(r_{\text{ij}})$ is the interatomic potential (r_{ij} being interatomic spacing); F_i is the embedding energy which in turn is a functional of the electron density function, $\rho_{\text{ij}} = \rho_{\text{ij}}(r_{\text{ij}})$. For NiTi binary alloy, one ought to incorporate the following functions to fully describe the bonding energy landscape: F_{Ni}, F_{Ti}, $\rho_{\text{Ni-Ni}}$, $\rho_{\text{Ti-Ti}}$, $\rho_{\text{Ni-Ti}}$, $\varphi_{\text{Ni-Ni}}$, $\varphi_{\text{Ti-Ti}}$ and $\varphi_{\text{Ni-Ti}}$. The terms representing the pure species are accurately modelled by Mishin and co-workers [35,36], which only leave the interspecies $\rho_{\text{Ni-Ti}}$ and $\varphi_{\text{Ni-Ti}}$ to be established as follows.

Within a cut-off distance of 0.52 nm (which incorporates fourth nearest neighbours in B2 lattice), both $\rho_{\text{Ni-Ti}}$ and $\varphi_{\text{Ni-Ti}}$ are modelled as cubic spline of the form:

$$\rho(r) \text{ or } \phi(r) = \sum_{\alpha} a_{\alpha}(r_{\alpha} - r)^3 \text{H}(r_{\alpha} - r) \tag{2}$$

where α denotes a particular knot; the Heaviside function, $\text{H}(r - r_{\alpha}) = 1$ for $(r - r_{\alpha}) \geq 0$ and $\text{H}(r - r_{\alpha}) = 0$ for $(r - r_{\alpha}) < 0$. The coefficients a_{α} are determined at known r_{α} values up to the cut-off radius by optimization method. First an objective function (Z) considering the fitting weight (w_{β}) is defined, to be minimized:

$$Z = \sum_{\beta} w_{\beta}\left(Y\left(r, a_{\beta}\right) - Y_{\beta 0}\right) \tag{3}$$

where $Y_{\beta 0}$ is the target value (e.g. elastic constant, energy from experiments and DFT predictions) and $Y\left(r, a_{\beta}\right)$ is fitting value with an adjustable a_{β}. With w_{β} set manually, a_{β} values corresponding to the minimized Z is determined and plugged back in Equation (2), thus, numerically reconstructing the $\rho_{\text{Ni-Ti}}$ and $\varphi_{\text{Ni-Ti}}$ functions. Using the foregoing methodology, the target database to be fitted includes: (a) the energy versus volume relations for B2, B19, B19′, BCO (body-centred

orthogonal) crystals and imaginary compounds, B1-NiTi, $L1_2$-Ni_3Ti and $L1_2$-$NiTi_3$, as obtained from *Quantum Espresso*-based predictions [37], (b) experimentally determined B2 elastic constants (C_{11}, C_{12} and C_{44}) [38] and (c) cohesive energies for pure species [35,36]. Reasonably good agreement with DFT predictions and experiments (where available) is observed, for example, in terms of elastic moduli of both B2 and B19′ crystals (Tables A1 and A2). The accurate modelling of the elastic moduli has contributed to the realistic predictions (comparable to experimentally observed ones) of the stress–strain hysteresis loops.

Table A1. Comparison of elastic constants (in GPa) of B19′ from the current potential, literature potential (by Zhong et al. [15]), and DFT predictions [39].

		B19′	
Elastic constants (GPa)	Current potential	Literature DFT [39]	Literature potential [15]
C_{11}	206	209	692
C_{12}	72	114	400
C_{13}	103	102	326
C_{15}	2	1	292
C_{22}	252	234	1135
C_{23}	120	139	222
C_{25}	−7	−7	125
C_{33}	218	238	303
C_{35}	−16	27	175
C_{44}	37	77	286
C_{46}	−2	−5	110
C_{55}	41	23	215
C_{66}	43	72	114
Bulk modulus, B	141	154	447
Shear, modulus, μ	50	56	202
Young's modulus, E	133	150	526
Poisson's ratio, υ	0.34	0.34	0.3

Table A2. Comparison of elastic constants (in GPa) for B2 crystal from current potential, literature potential (by Zhong et al. [15]) and experiment [38].

		B2	
Elastic constants (GPa)	Current potential	Literature experiment [38]	Literature potential [15]
C11	146	162	205
C12	122	129	136
C44	35	35	47
Bulk modulus,B	130	140	159
Shear, modulus, μ	26	28	42
Young's modulus, E	73	78	116
Poisson's ratio, υ	0.41	0.41	0.38

Conducting MD simulations

The present simulations were performed using the open-source software LAMMPS [40] (*Large-scale Atomic/Molecular Massively Parallel Simulator*) (http://lammps.sandia.gov). The atomic configuration viewer Ovito [41] (http://ovito.org) was used to reveal the crystal phase transformation processes.

On defining the atomic positions, the crystal structure is first energetically minimized via the conjugate gradient energy algorithm. An isoenthalpic–isobaric ensemble was employed for non-equilibrium deformation simulations with a constant number of atoms and zero external pressure. A thermostat algorithm is utilized to maintain a steady absolute temperature prior to each non-equilibrium dynamics simulation. A Velocity Verlet time-integration scheme was used to conduct the time-step advancement during the deformation simulations. Further details of MD algorithm adopted for the ensemble averaging can be found at [42].